PHYSICAL REVIEW D **94,** 013011 (2016)

QCD and electroweak corrections to ZZ + jet production with Z-boson leptonic decays at the LHC

Wang Yong,[1] Zhang Ren-You,[1,*] Ma Wen-Gan,[1] Li Xiao-Zhou,[1] and Guo Lei[2]

[1]*Department of Modern Physics, University of Science and Technology of China (USTC), Hefei 230026, Anhui, People's Republic of China*

[2]*Department of Physics, Chongqing University, Chongqing 401331, People's Republic of China*

(Received 8 June 2016; published 18 July 2016)

In this paper we present the full next-to-leading-order (NLO) QCD + NLO electroweak (EW) corrections to the Z-boson pair production in association with a hard jet at the LHC. The subsequent Z-boson leptonic decays are included by adopting both the naive narrow-width approximation and MADSPIN methods for comparison. Since the ZZ + jet production is an important background for single Higgs boson production and new physics searches at hadron colliders, the theoretical predictions with high accuracy for the hadronic production of ZZ + jet are necessary. We present the numerical results of the integrated cross section and various kinematic distributions of final particles, and conclude that it is necessary to take into account the spin correlation and finite-width effects from the Z-boson leptonic decays. We also find that the NLO EW correction is quantitatively non-negligible in matching the experimental accuracy at the LHC, particularly in the high-transverse-momentum region.

DOI: 10.1103/PhysRevD.94.013011

I. INTRODUCTION

Weak gauge boson pair production with subsequent leptonic decays plays an essential role in the research of the Higgs particle and new physics beyond the standard model (SM). It is usually accompanied by one or more additional hard QCD radiations at the Large Hadron Collider (LHC), and therefore the study of VV' + jet(s) $(VV' = WW, ZZ, ZW)$ productions at the LHC is significantly important and may also help us to gain a deeper understanding of jet physics. The VV' + jet production cross sections are known up to the QCD next-to-leading order (NLO), and the precision calculations for the NLO QCD + NLO electroweak (EW) corrections are urgently needed to match the experimental accuracy at the LHC. These research items are listed in the 2013 Les Houches high precision wish list [1].

The Z-boson pair production is of great phenomenological importance in measuring gauge couplings at the LHC to test the gauge principle of the SM and search for new physics at the TeV scale. It is also one of the background processes for single Higgs boson production. Thus a thorough understanding of Z-boson pair production is necessary. So far physicists have made enormous efforts in investigating Z-boson pair production at hadron colliders, not only experimentally (see Refs. [2,3] and more references therein) but also theoretically. The NLO QCD predictions for Z-boson pair production were calculated in Ref. [4], and the next-to-next-to-leading-order QCD calculations were given in Ref. [5] including the significant loop-induced gluon-fusion contributions [6]. The NLO EW corrections to Z-boson pair production were given in Ref. [7], and extended to include leptonic decays with the spin correlation effect in Ref. [8]. More recently, an investigation of four-lepton production including the full off-shell contributions from the intermediate Z bosons and photons was presented in Ref. [9].

Z-boson pair production at a hadron collider is always associated with one or more additional hard jets. The complete NLO QCD calculation for ZZ + jet production without Z-boson decays at the Tevatron and the LHC was presented in Ref. [10], while a precision study including the NLO QCD + NLO EW corrections on ZZ + jet production at hadron colliders with subsequent vector-boson decays is still desired [1]. In this work we report on the NLO QCD + NLO EW calculations for ZZ + jet production with Z-boson leptonic decays in the SM at hadron colliders. The rest of this paper is organized as follows. The calculation strategy is described in Sec. II. Numerical results of the integrated cross section and various kinematic distributions are presented in Sec. III. Finally, we give a short summary in Sec. IV.

II. CALCULATION STRATEGY

A. General description

In this section we mainly describe the NLO EW corrections to the $pp \to ZZ$ + jet process, while the NLO QCD calculation has been accomplished in Ref. [10]. In both the NLO QCD and NLO EW calculations we apply FEYNARTS-3.7 [11] to generate the Feynman diagrams and FORMCALC-7.3 [12] to algebraically simplify the corresponding amplitudes. To check the correctness of our NLO QCD calculation, we perform the NLO QCD

*Corresponding author.
zhangry@ustc.edu.cn

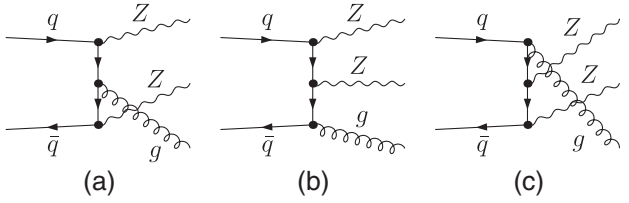

FIG. 1. Representative LO Feynman diagrams for the partonic process $q\bar{q} \to ZZg$.

calculation by using both FEYNARTS-3.7+FORMCALC-7.3+LOOPTOOLS-2.8 [11–13] and MADGRAPH5 [14], and find that the numerical results obtained from the two packages are in agreement within the calculation errors.

At the leading order (LO), the $pp \to ZZ + \text{jet} + X$ process involves the following partonic processes:

$$q\overline{q} \to ZZg, \qquad qg \to ZZq, \qquad \overline{q}g \to ZZ\overline{q}. \tag{2.1}$$

Some representative LO Feynman diagrams for the subprocess $q\overline{q} \to ZZg$ are shown in Fig. 1. In initial-state parton convolution we adopt the five-flavor scheme, i.e., $q = u, d, c, s, b$, and neglect their quark masses. In the NLO calculations we employ the dimensional regularization scheme to isolate both ultraviolet (UV) and infrared (IR) singularities. It is noteworthy that there is no need to distinguish the $ZZ + \text{jet}$ and $ZZ + \gamma$ events in the LO calculation, while we should properly define the $ZZ + \text{jet}$ event in the NLO EW calculation due to a possible additional photon in the final state. This issue will be detailed in Sec. II D.

The photon-induced subprocesses

$$\gamma q \to ZZq, \qquad \gamma\overline{q} \to ZZ\overline{q} \tag{2.2}$$

also contribute to the parent process $pp \to ZZ + \text{jet} + X$. In Fig. 2 we present the representative tree-level Feynman diagrams for the $\gamma q \to ZZq$ partonic process. Since the NLO QCD corrections to the photon-induced subprocesses are at $\mathcal{O}(\alpha^3\alpha_s)$ (the same order as the EW corrections to the quark-antiquark annihilation and quark-gluon fusion subprocesses), we should also include these photon-induced contributions in the calculation of the NLO QCD + EW corrections to $ZZ + \text{jet}$ production.

Now we clarify the appropriate choice of the fine-structure constant α in this work. The renormalized electric charge is given by

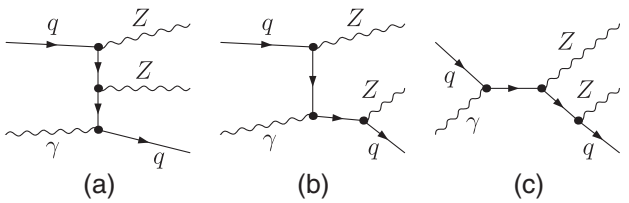

FIG. 2. Representative tree-level Feynman diagrams for the photon-induced subprocess $\gamma q \to ZZq$.

$$e_0 = (1 + \delta Z_e)e, \tag{2.3}$$

where e_0 is the bare electric charge and δZ_e is the corresponding renormalization constant. In the $\alpha(0)$ scheme, the on-shell renormalization condition is employed for the $e - e - \gamma$ vertex in the Thomson limit (photon momentum transfer $k^2 \to 0$). Then we get the electric charge renormalization constant as [15]

$$\delta Z_e^{\alpha(0)} = -\frac{1}{2}\delta Z_{AA} - \frac{\sin\theta_W}{\cos\theta_W}\frac{1}{2}\delta Z_{ZA}, \tag{2.4}$$

where the wave-function renormalization constants δZ_{AA} and δZ_{ZA} are given by

$$\delta Z_{AA} = -\left.\frac{\partial \sum_T^{AA}(k^2)}{\partial k^2}\right|_{k^2\to 0}, \qquad \delta Z_{ZA} = 2\frac{\sum_T^{AZ}(0)}{M_Z^2}. \tag{2.5}$$

$\sum_T^{XY}(k^2)$ is the transverse part of the unrenormalized self-energy of the $X \to Y$ transition at momentum squared k^2. As we know, the electric charge renormalization constant $\delta Z_e^{\alpha(0)}$ contains mass-singular terms $\log(m_f^2/\mu^2)$ $(f = e, \mu, \tau, u, d, c, s, b)$. For a process with l external photons and n EW couplings in the tree-level amplitude, if $l = n$, the full NLO EW correction is free of those unpleasant large logarithms because of the exact cancellation between the logarithms in vertex counterterms and in external photon wave-function counterterms; however, if $l < n$, the uncanceled large logarithms can be absorbed into $n - l$ EW couplings by using a running fine-structure constant as input for these $n - l$ EW vertices. Therefore, we adopt the G_μ scheme for all the EW couplings of the $pp \to ZZ + \text{jet} + X$ process in our calculation. In the G_μ scheme, the fine-structure constant is chosen as

$$\alpha_{G_\mu} = \frac{\sqrt{2}}{\pi}G_\mu M_W^2 \sin^2\theta_W \tag{2.6}$$

to absorb those large logarithmic corrections in $\delta Z_e^{\alpha(0)}$. Correspondingly, the electric charge renormalization constant in the G_μ scheme should be modified as

$$\delta Z_e^{G_\mu} = \delta Z_e^{\alpha(0)} - \frac{1}{2}\Delta r, \tag{2.7}$$

where Δr is provided in Ref. [16] by considering the one-loop EW corrections to muon decay. This subtraction term is introduced to avoid double counting in the NLO EW calculation.

B. Virtual EW corrections

The $\mathcal{O}(\alpha^3\alpha_s)$ correction to the parent process $pp \to ZZ + \text{jet} + X$ includes two parts: (1) NLO EW corrections to the quark-antiquark annihilation and quark-gluon fusion

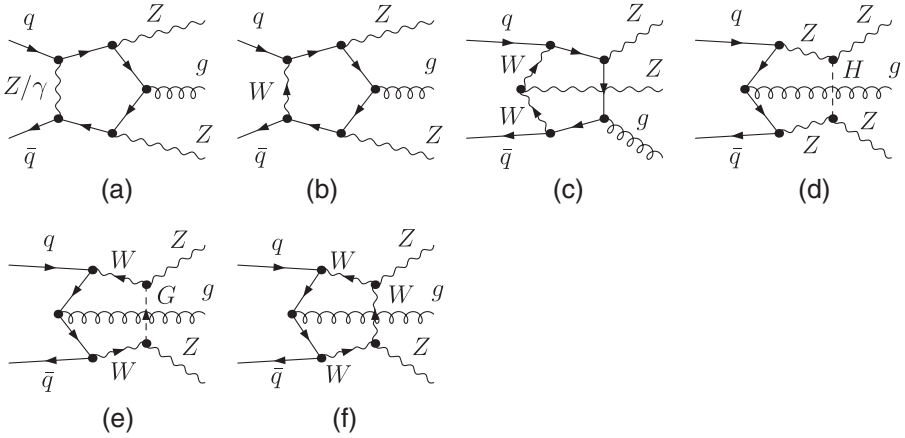

FIG. 3. Representative EW pentagon diagrams for the partonic process $q\bar{q} \to ZZg$.

partonic channels (2.1), and (2) NLO QCD corrections to the photon-induced subprocesses (2.2). The virtual corrections are induced by the related self-energy, vertex, box, and pentagon graphs. In Fig. 3 we depict the representative EW pentagon diagrams for the partonic process $q\overline{q} \to ZZg$. The UV divergences can be canceled exactly after performing the renormalization procedure, and the mass singularities are also removed since the G_μ scheme is adopted in the electric charge renormalization. The IR divergences originating from virtual photon exchange in loops can be canceled after adding the real photon emission corrections and the EW counterterms of parton distribution functions (PDFs). Then the final results are UV and IR finite.

We follow the approach proposed by Denner and Dittmaier [17] to decompose five-point integrals into four-point integrals. All tensor integrals can be reduced to scalar integrals recursively by using the Passarino-Veltman algorithm [18]. In the numerical calculation of four-point integrals, we may confront a serious instability problem induced by the small Gram determinant. In order to solve this instability problem, we add the quadruple precision arithmetic option in LOOPTOOLS-2.8 [13] by using a segmentation method analogous to that in Refs. [19,20]. After the refinement above, the program can flexibly switch to the quadruple precision arithmetic in the region of $\det G_3/(2k^2_{\max})^3 < 10^{-5}$, where $\det G_3$ is the Gram determinant and $k^2_{\max}$ is the maximum of the external four-momentum squared for a given four-point integral. Finally, we successfully keep the numerical instability under control and consume relatively less computer CPU time.

C. Real photon emission corrections

The real photon emission corrections to the partonic channels in Eq. (2.1) are from the following subprocesses:

$$q\overline{q} \to ZZg\gamma, \qquad qg \to ZZq\gamma, \qquad \overline{q}g \to ZZ\overline{q}\gamma. \tag{2.8}$$

The soft and collinear IR divergences in real photon emission corrections are canceled exactly and partially with those from loop diagrams, respectively, and the remaining collinear IR singularities are absorbed by the EW counterterms of quark PDFs. The quark PDF EW counterterm $\delta\Phi^{\rm EW}_{q|P}$ contains two parts: the collinear photon emission part $\delta\Phi^{{\rm EW},(\gamma)}_{q|P}$ and the collinear light-quark emission part $\delta\Phi^{{\rm EW},(q)}_{q|P}$. In the dimensional regularization and deep inelastic scattering (DIS) factorization scheme, these two collinear parts are expressed as

$$\begin{aligned}
&\delta\Phi^{{\rm EW},(\gamma)}_{q|P}(x,\mu_f,\mu_r) \\
&\quad = \frac{Q_q^2\alpha}{2\pi}\int_x^1 \frac{dz}{z}\Phi_{q|P}(x/z,\mu_f) \\
&\qquad \times\left\{\frac{1}{\epsilon}\frac{\Gamma(1-\epsilon)}{\Gamma(1-2\epsilon)}\left(\frac{4\pi\mu_r^2}{\mu_f^2}\right)^{\epsilon}[P_{qq}(z)]_+ - C^{\rm DIS}_{qq}(z)\right\}, \\
&\delta\Phi^{{\rm EW},(q)}_{q|P}(x,\mu_f,\mu_r) \\
&\quad = \frac{3Q_q^2\alpha}{2\pi}\int_x^1 \frac{dz}{z}\Phi_{\gamma|P}(x/z,\mu_f) \\
&\qquad \times\left\{\frac{1}{\epsilon}\frac{\Gamma(1-\epsilon)}{\Gamma(1-2\epsilon)}\left(\frac{4\pi\mu_r^2}{\mu_f^2}\right)^{\epsilon}P_{q\gamma}(z) - C^{\rm DIS}_{q\gamma}(z)\right\},
\end{aligned} \tag{2.9}$$

where Q_q is the electric charge of quark q. The splitting functions $P_{ij}(z)$ are written as

$$P_{qq} = \frac{1+z^2}{1-z}, \qquad P_{q\gamma}(z) = z^2 + (1-z)^2, \tag{2.10}$$

and the DIS subtraction functions $C^{\rm DIS}_{ij}(z)$ are given by [19,21]

$$\begin{aligned}
C^{\rm DIS}_{qq}(z) &= \left[P_{qq}(z)\left(\ln\frac{1-z}{z} - \frac{3}{4}\right) + \frac{9+5z}{4}\right]_+, \\
C^{\rm DIS}_{q\gamma}(z) &= P_{q\gamma}(z)\ln\frac{1-z}{z} - 8z^2 + 8z - 1.
\end{aligned} \tag{2.11}$$

The $[\ldots]_+$ prescription is understood as

$$\int_0^1 dz[g(z)]_+ f(z) = \int_0^1 dz g(z)[f(z) - f(1)]. \quad (2.12)$$

In calculating real photon emission partonic processes, we employ the two cutoff phase-space slicing (TCPSS) method [22] to isolate the soft and collinear IR singularities. By introducing two arbitrary small cutoffs δ_s and δ_c, the phase space of a real photon emission process is decomposed into soft ($E_\gamma \le \delta_s\sqrt{\hat{s}}/2$), hard collinear ($E_\gamma > \delta_s\sqrt{\hat{s}}/2$, $\min\{\hat{s}_{\gamma f}\} \le \delta_c\hat{s}$), and hard noncollinear ($E_\gamma > \delta_s\sqrt{\hat{s}}/2$, $\min\{\hat{s}_{\gamma f}\} > \delta_c\hat{s}$) regions, where $\sqrt{\hat{s}}$ is the partonic center-of-mass colliding energy, $\hat{s}_{ij} = (p_i + p_j)^2$, and f runs over the charged fermions in initial and final states. The soft and collinear IR singularities are located in the soft and hard collinear regions, respectively, while the phase-space integration over the hard noncollinear region is IR finite. The cutoff independence of the real photon emission corrections has been checked numerically in the range of $10^{-6} < \delta_s < 10^{-3}$ with $\delta_c = \delta_s/50$.

D. Event identification and selection

For inclusive $ZZ+$jet production, there exist $ZZ+$jet $+$ jet and $ZZ+$jet $+\gamma$ four-particle events originating from the real gluon, light-quark, and photon emissions at $\mathcal{O}(\alpha^2\alpha_s^2)$ and $\mathcal{O}(\alpha^3\alpha_s)$. The topologies of these real emission subprocesses are expressed as

$$0 \to ZZq\bar{q}gg, \qquad 0 \to ZZq\bar{q}q'\bar{q}', \qquad 0 \to ZZq\bar{q}g\gamma. \quad (2.13)$$

We apply the transverse momentum cut of

$$p_{T,\mathrm{jet}} > p_{T,\mathrm{jet}}^{\mathrm{cut}} \quad (2.14)$$

on the leading jet of the final state to ensure a detectable hard jet in the inclusive $ZZ+$jet production. This kinematic cut can also guarantee the IR safety at the LO. If the two tracks of jets (or jet and photon) of the final state are sufficiently collinear—i.e., R_{jetjet} (or $R_{\gamma\mathrm{jet}}$) $< R_0$, where $R_{ij} = \sqrt{(y_i - y_j)^2 + (\phi_i - \phi_j)^2}$ represents the separation of the two tracks on the rapidity-azimuthal-angle plane—we merge them into a single jet track. However, this naive track combination procedure is always accompanied by two problems for $0 \to ZZq\bar{q}g\gamma$ if the final state is $ZZ+$jet $+\gamma$. First, the $0 \to ZZq\bar{q}g\gamma$ topology with the $ZZ+$jet $+\gamma$ final state [i.e., the partonic processes in Eq. (2.8)] can be treated as not only the real photon bremsstrahlung to the $ZZ+$jet production but also the real jet emission to the $ZZ+\gamma$ production. Therefore, the jet-photon-merged track might be regarded as a photon, and not necessarily a jet. Second, for the $q\bar{q} \to ZZg\gamma$ subprocess, if the gluon-photon-merged track is regarded as a jet, the energy fraction of the gluon inside the jet can be arbitrarily small even if the jet selection criterion (2.14) is applied. This soft gluon induces an unexpected QCD soft IR singularity that cannot be canceled at the EW NLO.

To solve these two problems we introduce an event selection criterion for the $pp \to ZZ+$jet $+\gamma + X$ process in which $ZZ+$jet and $ZZ+\gamma$ events are properly defined. In the case that $R_{\gamma\mathrm{jet}} < R_0$, the jet and photon tracks are merged into a single track and the final state is a three-particle event. If $z_\gamma > z_\gamma^{\mathrm{cut}}$, where z_γ is the energy fraction of the photon inside the merged track, this three-particle event is called a $ZZ+\gamma$ event and rejected; otherwise, it is treated as a $ZZ+$jet event and kept [23]. However, this event selection criterion leads to the uncanceled final-state QED collinear IR divergence from the $qg \to ZZq\gamma$ and $\bar{q}g \to ZZ\bar{q}\gamma$ partonic processes in the region of $z_\gamma \in (z_\gamma^{\mathrm{cut}}, 1]$. In analogy to the absorption of initial-state collinear IR singularities into PDFs, this remaining QED collinear IR divergence can be absorbed into the NLO definition of the quark-to-photon fragmentation function.

At the EW NLO, the bare quark-to-photon fragmentation function in the $\overline{\mathrm{MS}}$ renormalization scheme can be written as [24]

$$D_{q\to\gamma}^{\mathrm{bare}}(z_\gamma) = \frac{Q_q^2\alpha}{2\pi}\frac{1}{\epsilon}\frac{1}{\Gamma(1-\epsilon)}\left(\frac{4\pi\mu_r^2}{\mu_f^2}\right)^\epsilon P_{\gamma q}(z_\gamma) + D_{q\to\gamma}(z_\gamma, \mu_f), \quad (2.15)$$

where the quark-to-photon splitting function $P_{\gamma q}(z_\gamma)$ is given by

$$P_{\gamma q}(z_\gamma) = \frac{1 + (1 - z_\gamma)^2}{z_\gamma}. \quad (2.16)$$

The nonperturbative fragmentation function $D_{q\to\gamma}(z_\gamma, \mu_f)$ is experimentally feasible and has been measured at LEP in $\gamma+$jet events. In this paper, we employ the parametrization of the nonperturbative fragmentation function used by the ALEPH Collaboration [25], i.e.,

$$D_{q\to\gamma}(z_\gamma, \mu_f) = D_{q\to\gamma}^{\mathrm{ALEPH}}(z_\gamma, \mu_f) \equiv \frac{Q_q^2\alpha}{2\pi}\left(P_{\gamma q}(z_\gamma)\ln\frac{\mu_f^2}{(1-z_\gamma)^2\mu_0^2} + C\right), \quad (2.17)$$

where $\mu_0 = 0.14$ GeV and $C = -1 - \ln(M_Z^2/2\mu_0^2) = -13.26$ are obtained from a one-parameter data fit.

According to the event selection criterion described above, we should subtract the contribution of the $ZZ+\gamma$ events from the perturbatively well-defined inclusive cross section in which the photon energy fraction z_γ ranges over $0 \le z_\gamma \le 1$. The subtraction term can be written as

$$d\sigma^{(\mathrm{sub})} = d\sigma^{(\mathrm{pert})}_{\mathrm{fin}} + [d\sigma^{(\mathrm{pert})}_{\mathrm{sing}} + d\sigma^{(\mathrm{frag})}], \quad (2.18)$$

where $d\sigma^{(\mathrm{pert})}$ and $d\sigma^{(\mathrm{frag})}$ correspond to the perturbative radiation and nonperturbative production of a photon over the region of $z_\gamma \in (z_\gamma^{\mathrm{cut}}, 1]$, and the subscripts "fin" and "sing" denote the collinear-safe and -singular parts, respectively. By employing the TCPSS method, the two terms on the right-hand side of Eq. (2.18) can be expressed as

$$\begin{aligned} d\sigma^{(\mathrm{pert})}_{\mathrm{fin}} &= \sum_{q=u,d,c,s,b} \int_{z_{\mathrm{cut}}}^{1} [d\sigma^{\mathrm{LO}}(pp \to q\bar{q} \to ZZ + \mathrm{jet} + \gamma)|_{R_{\gamma\mathrm{jet}} < R_0} \\ &\quad + d\sigma^{\mathrm{LO}}(pp \to qg, \bar{q}g \to ZZ + \mathrm{jet} + \gamma)|_{R_{\gamma\mathrm{jet}} < R_0, \hat{s}_{\gamma\mathrm{jet}} > \delta_c \hat{s}}], \\ [d\sigma^{(\mathrm{pert})}_{\mathrm{sing}} + d\sigma^{(\mathrm{frag})}] &= \sum_{q=u,d,c,s,b} d\sigma^{\mathrm{LO}}(pp \to qg, \bar{q}g \to ZZ + \mathrm{jet}) \int_{z_{\mathrm{cut}}}^{1} dz_\gamma \mathcal{D}_{q\to\gamma}(z_\gamma), \end{aligned} \quad (2.19)$$

where the (collinear-safe) effective quark-to-photon fragmentation function $\mathcal{D}_{q\to\gamma}(z_\gamma)$ is defined as [24]

$$\begin{aligned} \mathcal{D}_{q\to\gamma}(z_\gamma) = &-\frac{Q_q^2 \alpha}{2\pi} \frac{1}{\epsilon} \frac{1}{\Gamma(1-\epsilon)} \left(\frac{4\pi\mu_r^2}{\delta_c \hat{s}}\right)^{\epsilon} \\ &\times [z_\gamma(1-z_\gamma)]^{-\epsilon} [P_{\gamma q}(z_\gamma) - \epsilon z_\gamma] + D^{\mathrm{bare}}_{q\to\gamma}(z_\gamma). \end{aligned} \quad (2.20)$$

As shown in Eqs. (2.18), (2.19), and (2.20), the subtraction term $d\sigma^{(\mathrm{sub})}$ is collinear safe, and therefore a (UV- and) IR-finite NLO QCD + EW corrected cross section for $pp \to ZZ + \mathrm{jet} + X$ is obtained after applying the $ZZ+$jet event selection criterion.

III. NUMERICAL RESULTS AND DISCUSSION

A. Input parameters and setup

The relevant SM input parameters are [26]

$$\begin{aligned} &M_W = 80.385\ \mathrm{GeV}, \quad M_Z = 91.1876\ \mathrm{GeV}, \\ &M_H = 125.7\ \mathrm{GeV}, \quad m_e = 0.510998928\ \mathrm{MeV}, \\ &m_\mu = 105.6583715\ \mathrm{MeV}, \quad m_\tau = 1.77682\ \mathrm{GeV}, \\ &m_t = 173.21\ \mathrm{GeV}, \quad G_\mu = 1.1663787 \times 10^{-5}\ \mathrm{GeV}^{-2}, \\ &\alpha_s(M_Z) = 0.119. \end{aligned} \quad (3.1)$$

If the Cabibbo-Kobayashi-Maskawa (CKM) matrix V_{CKM} is $2 \oplus 1$ block diagonal, i.e., only the quark mixing between the first two generations is taken into account, the LO and NLO corrected cross sections for $ZZ+$jet production are independent of the CKM matrix elements because all the related topologies[1] contain no charged-current quark chain. Therefore, we set $V_{\mathrm{CKM}} = \mathbf{1}_{3\times 3}$ in the numerical calculation.

[1]The topologies related to $ZZ+$jet production at QCD + EW NLO are $0 \to ZZq\bar{q}g$ and those in Eq. (2.13).

We employ the NLO NNPDF2.3QED PDFs [27] with $\overline{\mathrm{MS}}$ and DIS factorization schemes in the NLO QCD and EW calculations, respectively. The strong-coupling constant α_s is renormalized in the $\overline{\mathrm{MS}}$ scheme with five active flavors. The NLO QCD and EW corrections are expressed as

$$\begin{aligned} \Delta\sigma^{\mathrm{NLO\,QCD}} &= \sigma^{\alpha_s}_{\mathrm{virt}} + \sigma^{\alpha_s}_{\mathrm{real}} + \sigma^{\alpha_s}_{\mathrm{pdf}} + (\sigma^0 - \sigma^{\mathrm{LO}}), \\ \Delta\sigma^{\mathrm{NLO\,EW}} &= \sigma^{\alpha}_{\mathrm{virt}} + \sigma^{\alpha}_{\mathrm{real}} + \sigma^{\alpha}_{\mathrm{pdf}} - \sigma^{(\mathrm{sub})}, \end{aligned} \quad (3.2)$$

where $\sigma^{\alpha_s,\alpha}_{\mathrm{virt}}$, $\sigma^{\alpha_s,\alpha}_{\mathrm{real}}$, and $\sigma^{\alpha_s,\alpha}_{\mathrm{pdf}}$ are the virtual, real, and PDF-counterterm corrections at $\mathcal{O}(\alpha^2\alpha_s^2)$ and $\mathcal{O}(\alpha^3\alpha_s)$, respectively, and σ^{LO} and σ^0 are the LO cross sections calculated with the LO and NLO NNPDF2.3QED PDFs, respectively. As discussed in Sec. II A, we also include the contributions from the photon-induced subprocesses (2.2) up to $\mathcal{O}(\alpha^3\alpha_s)$, i.e.,

$$\sigma_{\gamma\text{-ind}} = \sigma^0_{\gamma\text{-ind}} + \Delta\sigma^{\mathrm{NLO\,QCD}}_{\gamma\text{-ind}}, \quad (3.3)$$

where $\sigma^0_{\gamma\text{-ind}}$ and $\Delta\sigma^{\mathrm{NLO\,QCD}}_{\gamma\text{-ind}}$ are Born and NLO QCD photon-induced contributions, respectively, both calculated with the NLO NNPDF2.3QED PDFs. Then the relative QCD, EW, and photon-induced corrections are given by

$$\begin{aligned} &\delta_{\mathrm{QCD}} = \frac{\Delta\sigma^{\mathrm{NLO\,QCD}}}{\sigma^{\mathrm{LO}}}, \qquad \delta_{\mathrm{EW}} = \frac{\Delta\sigma^{\mathrm{NLO\,EW}}}{\sigma^0}, \\ &\delta_{\gamma\text{-ind}} = \frac{\sigma_{\gamma\text{-ind}}}{\sigma^{\mathrm{LO}}}. \end{aligned} \quad (3.4)$$

To obtain the full NLO corrected cross section, we combine the QCD and EW corrections by using the naive product of the relative corrections and add the photon-induced contributions linearly [28], i.e.,

$$\sigma^{\mathrm{NLO}} = \sigma^{\mathrm{LO}}[(1+\delta_{\mathrm{QCD}})(1+\delta_{\mathrm{EW}})+\delta_{\gamma\text{-ind}}] = \sigma^{\mathrm{LO}}(1+\delta_{\mathrm{NLO}}). \quad (3.5)$$

The parameters for $ZZ+\mathrm{jet}$ event identification and selection are fixed as

$$R_0 = 0.5, \qquad z_{\mathrm{cut}} = 0.7, \qquad p_{T,\mathrm{jet}}^{\mathrm{cut}} = 50\ \mathrm{GeV}. \quad (3.6)$$

The factorization and renormalization scales are set to be equal ($\mu_f = \mu_r = \mu$) for simplicity, and the central scale value is chosen as

$$\mu_0 = H_T/2 = \sum m_T/2, \quad (3.7)$$

where $m_T = \sqrt{m^2+\vec{p}_T^{\,2}}$ is the transverse mass of a particle and the summation is taken over all the final particles for the process $pp \to ZZ + \mathrm{jet} + X$. In the following numerical calculation, we take $\mu = \mu_0$ by default unless otherwise stated. Compared to the fixed scale choice used in Ref. [10], this dynamic factorization/renormalization scale would be better able to capture information about the dynamics than the fixed one.

B. Integrated cross sections

In Table I we list the LO and NLO QCD + EW corrected integrated cross sections (including photon-induced contributions) and the corresponding relative corrections (δ_{QCD}, δ_{EW}, $\delta_{\gamma\text{-ind}}$, and δ_{NLO}) for $ZZ+\mathrm{jet}$ production at $\sqrt{S} = 13$, 14, 33, and 100 TeV hadron colliders separately. We can see from the table that the LO cross section is enhanced by the NLO QCD correction, while it is suppressed by the NLO EW correction. Although the LO cross section increases notably with the increment of the proton-proton colliding energy, both the relative QCD and EW corrections are insensitive to the colliding energy. The NLO EW correction is about 1 order of magnitude smaller than the NLO QCD correction but quantitatively not negligible, while the photon-induced correction is very small compared to both the NLO QCD and NLO EW corrections.

In Table II we demonstrate the $p_{T,\mathrm{jet}}^{\mathrm{cut}}$ dependence of the LO and NLO QCD + EW corrected integrated cross sections and the corresponding relative corrections for $ZZ+\mathrm{jet}$ production at the 14 TeV LHC. The table shows that both the QCD and EW relative corrections are sensitive to the transverse momentum cut on the hardest jet. With the increment of $p_{T,\mathrm{jet}}^{\mathrm{cut}}$, the LO cross section decreases quickly since the transverse momentum cut of $p_{T,\mathrm{jet}} > p_{T,\mathrm{jet}}^{\mathrm{cut}}$ is imposed on the hardest jet to select the $ZZ+\mathrm{jet}$ events, while the relative QCD correction increases due to the experimentally unresolved real jet radiation at the QCD NLO. Contrary to the QCD correction, the relative EW correction decreases with the increment of $p_{T,\mathrm{jet}}^{\mathrm{cut}}$, because the real photon emission would soften the final jet, and moreover, the final state is not a $ZZ+\mathrm{jet}$ event if the photon is unresolved and sufficiently energetic.

TABLE I. The LO and NLO QCD + EW corrected integrated cross sections and the corresponding relative corrections for $ZZ+\mathrm{jet}$ production at $\sqrt{S} = 13$, 14, 33, and 100 TeV proton-proton colliders.

$\sqrt{S}$ [TeV]	σ^{LO} [pb]	σ^{NLO} [pb]	δ_{QCD} [%]	δ_{EW} [%]	$\delta_{\gamma\text{-ind}}$ [%]	δ_{NLO} [%]
13	1.8709(1)	2.708(4)	52.6	−5.22	0.13	44.76
14	2.1348(3)	3.087(5)	52.6	−5.32	0.13	44.61
33	8.6670(8)	12.63(2)	54.4	−5.66	0.10	45.76
100	41.916(5)	60.45(8)	53.5	−6.10	0.07	44.21

TABLE II. The LO and NLO QCD + EW corrected integrated cross sections and the corresponding relative corrections for $ZZ+\mathrm{jet}$ production at the 14 TeV LHC by taking $p_{T,\mathrm{jet}}^{\mathrm{cut}} = 20$, 50, 100, and 200 GeV.

$p_{T,\mathrm{jet}}^{\mathrm{cut}}$ [GeV]	σ^{LO} [pb]	σ^{NLO} [pb]	δ_{QCD} [%]	δ_{EW} [%]	$\delta_{\gamma\text{-ind}}$ [%]	δ_{NLO} [%]
20	5.2701(6)	7.146(9)	42.0	−4.59	0.11	35.59
50	2.1348(3)	3.087(5)	52.6	−5.32	0.13	44.61
100	0.76528(7)	1.176(2)	65.2	−7.04	0.16	53.73
200	0.16125(2)	0.2759(4)	91.8	−10.91	0.20	71.07

To estimate the theoretical uncertainty from the factorization and renormalization scales, we define the upper and lower relative scale uncertainties as

$$\eta_{+,-} = \max,\min\left\{\frac{\sigma(\mu_f,\mu_r)}{\sigma(\mu_0,\mu_0)}\middle|\mu_f,\mu_r \in \{\mu_0/2, 2\mu_0\}\right\} - 1. \quad (3.8)$$

The LO and NLO QCD + EW corrected integrated cross sections combined with the scale uncertainties for $ZZ+\mathrm{jet}$ production at the 14 TeV LHC are given as

$$\sigma^{\mathrm{LO}} = 2.1348^{+9.8\%}_{-8.5\%}\ \mathrm{pb}, \qquad \sigma^{\mathrm{NLO}} = 3.087^{+5.5\%}_{-4.7\%}\ \mathrm{pb}. \quad (3.9)$$

It shows that the NLO QCD + EW correction can improve the accuracy of the integrated cross section by reducing the scale uncertainty.

C. Kinematic distributions

In this subsection we provide some kinematic distributions of final particles before and after the Z-boson leptonic decays at the 14 TeV LHC.

1. Distributions for $pp \to ZZ + \mathrm{jet} + X$

In Fig. 4(a) we present the LO and NLO QCD, and NLO QCD + EW corrected Z-pair invariant mass distributions ($\frac{d\sigma^{\mathrm{LO}}}{dM_{ZZ}}$, $\frac{d\sigma^{\mathrm{NLO\,QCD}}}{dM_{ZZ}}$, $\frac{d\sigma^{\mathrm{NLO}}}{dM_{ZZ}}$) and the corresponding relative corrections for $pp \to ZZ + \mathrm{jet} + X$. From the figure we see

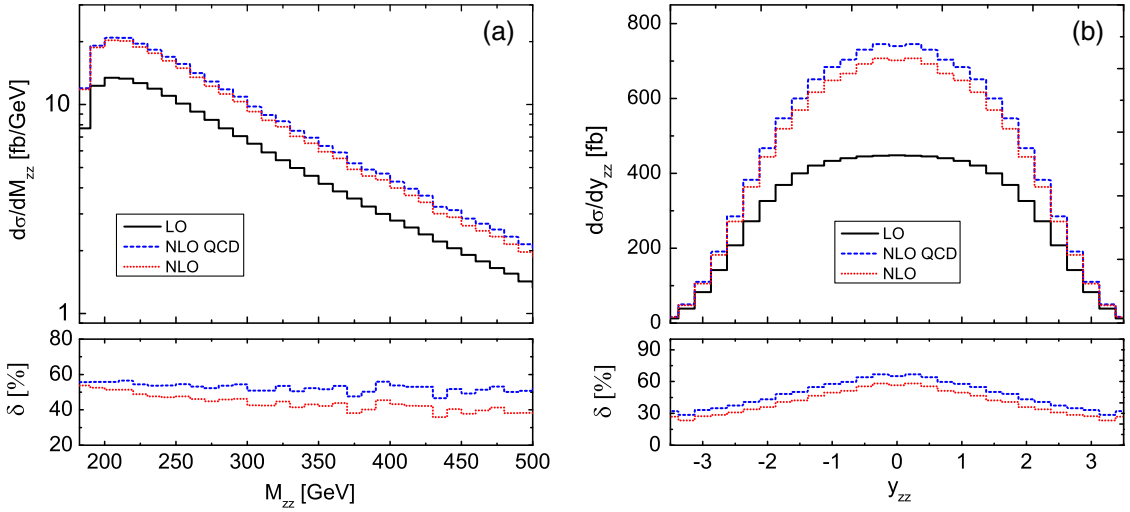

FIG. 4. The LO and NLO QCD and NLO QCD + EW corrected (a) invariant mass and (b) rapidity distributions of the Z-boson pair for $pp \to ZZ + \text{jet} + X$ at the 14 TeV LHC.

that the NLO QCD and EW corrections do not distort the line shape of the LO M_{ZZ} distribution. The NLO QCD correction enhances the LO M_{ZZ} distribution significantly, while the NLO EW correction is small compared to the NLO QCD correction and slightly suppresses the LO M_{ZZ} distribution. Both the LO and NLO corrected M_{ZZ} distributions reach their maxima in the vicinity of $M_{ZZ} \sim 200$ GeV, and then decrease rapidly with the increment of M_{ZZ}. In the plotted M_{ZZ} region, the relative QCD correction is stable, while the relative EW correction decreases from -1.24% to -8.30% with the increment of M_{ZZ}. The NLO EW correction becomes relatively significant in the high-M_{ZZ} region due to the large EW Sudakov logarithms [29]. The full NLO (QCD + EW) relative correction decreases from 53.7% to 38.3% with the increment of M_{ZZ} from its threshold to 500 GeV.

The LO and NLO QCD and NLO QCD + EW corrected rapidity distributions of the Z-boson pair ($\frac{d\sigma^{\text{LO}}}{dy_{ZZ}}$, $\frac{d\sigma^{\text{NLO QCD}}}{dy_{ZZ}}$, and $\frac{d\sigma^{\text{NLO}}}{dy_{ZZ}}$) are depicted in Fig. 4(b), and the corresponding relative corrections are plotted in the lower panel. We see clearly that the relative QCD correction is positive and decreases with the increment of $|y_{ZZ}|$, while the relative EW correction is insensitive to y_{ZZ} and suppresses the LO y_{ZZ} distribution a little bit in the whole plotted y_{ZZ} region. At $y_{ZZ} = 0$ and ± 3, the relative QCD corrections are 65.1% and 33.1%, while the relative EW corrections are

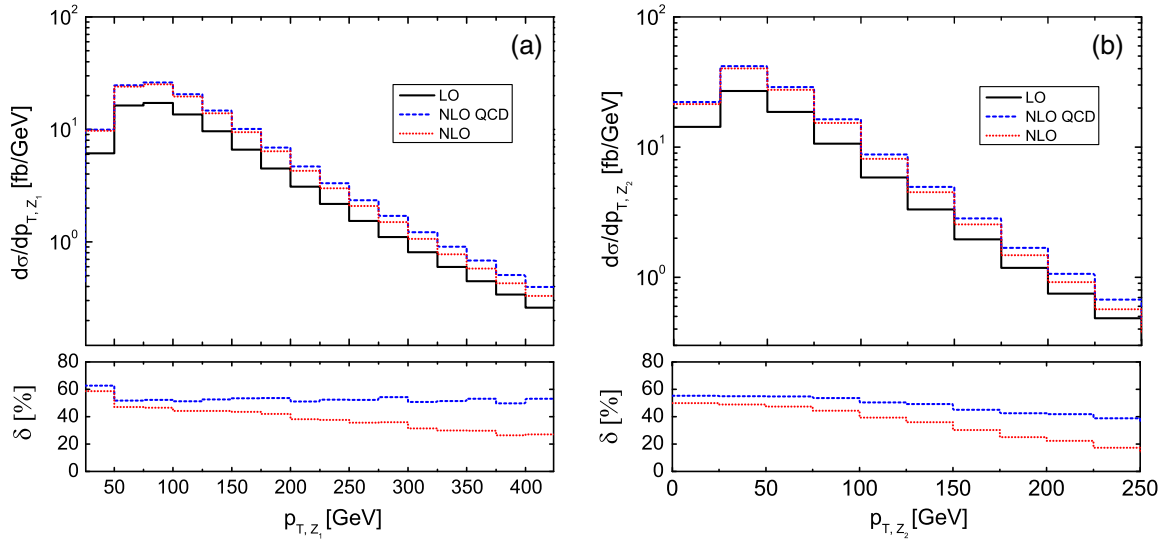

FIG. 5. The LO, NLO QCD and NLO QCD + EW corrected transverse momentum distributions of (a) leading and (b) second Z bosons for $pp \to ZZ + \text{jet} + X$ at the 14 TeV LHC.

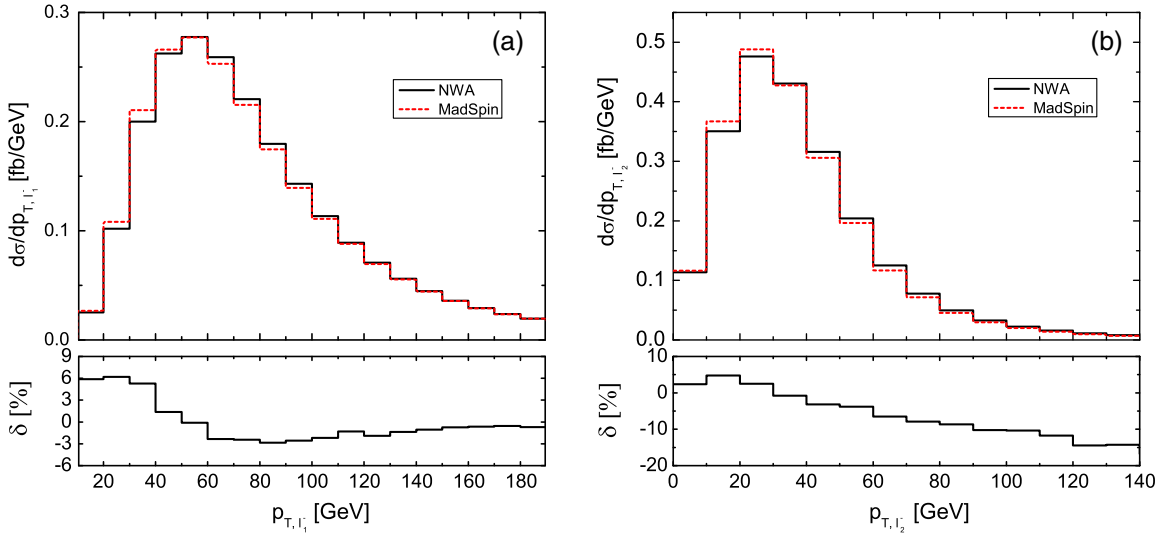

FIG. 6. The LO transverse distributions of (a) leading and (b) second negatively charged leptons for $pp \to ZZ + \text{jet} \to \ell^+\ell^-\ell'^+\ell'^- + \text{jet} + X$ at the 14 TeV LHC.

-5.18% and -4.30%, respectively. Consequently, we get the full NLO relative correction as 56.5% at $y_{ZZ} = 0$ and 27.4% at $|y_{ZZ}| = 3$.

Among the two final Z bosons, the leading Z boson Z_1 and the second Z boson Z_2 are defined as

$$p_{T,Z_1} > p_{T,Z_2}. \tag{3.10}$$

Their transverse momentum distributions and the corresponding relative corrections are shown in Figs. 5(a) and 5(b) separately. We see that both the LO and NLO corrected transverse momentum distributions peak at $p_{T,Z_1} \sim 75$ GeV and $p_{T,Z_2} \sim 25$ GeV for the leading and second Z bosons, respectively. The relative QCD correction is steady at about 50% in the plotted p_{T,Z_1} region for the leading Z boson, while it decreases from 55.2% to 38.8% as p_{T,Z_2} increases from 0 to 250 GeV for the second Z boson. However, the relative EW corrections to both the p_{T,Z_1} and p_{T,Z_2} distributions decrease, from -2.46% to -17.0% and from -3.45% to -15.5%, respectively, with the increment of p_{T,Z_1} and p_{T,Z_2} in their plotted regions. In analogy to the M_{ZZ} distribution, the large relative EW correction in the high-p_T region is due to the EW Sudakov effect. Consequently, the NLO QCD + EW correction enhances the LO transverse momentum distributions of the leading and second Z bosons, and the corresponding NLO relative corrections decrease from 58.7% to 27.1% and from 49.9% to 17.3%, respectively, with the increment of $p_{T,Z_1} \in [25, 425]$ GeV and $p_{T,Z_2} \in [0, 250]$ GeV.

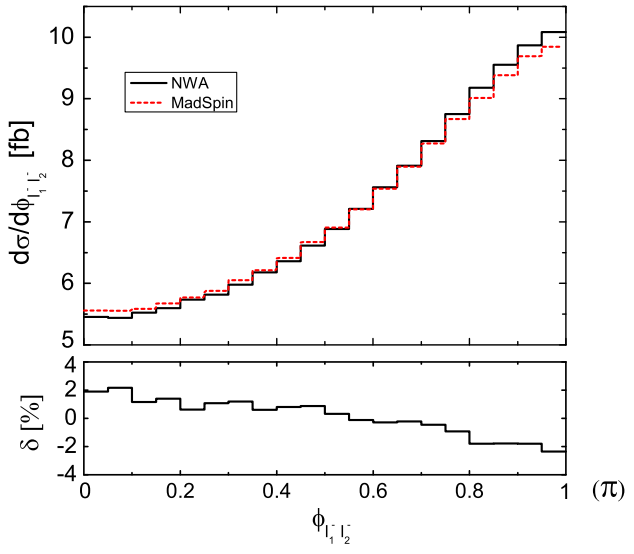

FIG. 7. The LO distributions of the azimuthal angle between the two negatively charged leptons for $pp \to ZZ + \text{jet} \to \ell^+\ell^-\ell'^+\ell'^- + \text{jet} + X$ at the 14 TeV LHC.

2. *Distributions for* $pp \to ZZ + \text{jet} \to 4\ell + \text{jet} + X$

Now we turn to $ZZ + \text{jet}$ production with subsequent Z-boson leptonic decays, i.e., $pp \to ZZ + \text{jet} \to \ell^+\ell^-\ell'^+\ell'^- + \text{jet} + X(\ell, \ell' = e, \mu, \tau)$, at the 14 TeV LHC. For each same-sign lepton pair in the final state ($\ell^+\ell'^+$ or $\ell^-\ell'^-$), the lepton with larger transverse momentum is called the leading lepton ℓ_1 and the other is called the second lepton ℓ_2. In the following we provide and discuss the distributions of the transverse momenta and azimuthal-angle separation of the two negatively charged leptons, i.e., $\frac{d\sigma}{dp_{T,\ell_1^-}}$, $\frac{d\sigma}{dp_{T,\ell_2^-}}$ and $\frac{d\sigma}{d\phi_{\ell_1^-\ell_2^-}}$.

In dealing with the sequential Z-boson decays one can use the naive narrow-width approximation (NWA). In this method, the final lepton pairs are produced isotropically by the on-shell Z-boson decays in the center-of-mass system without considering the spin correlation information

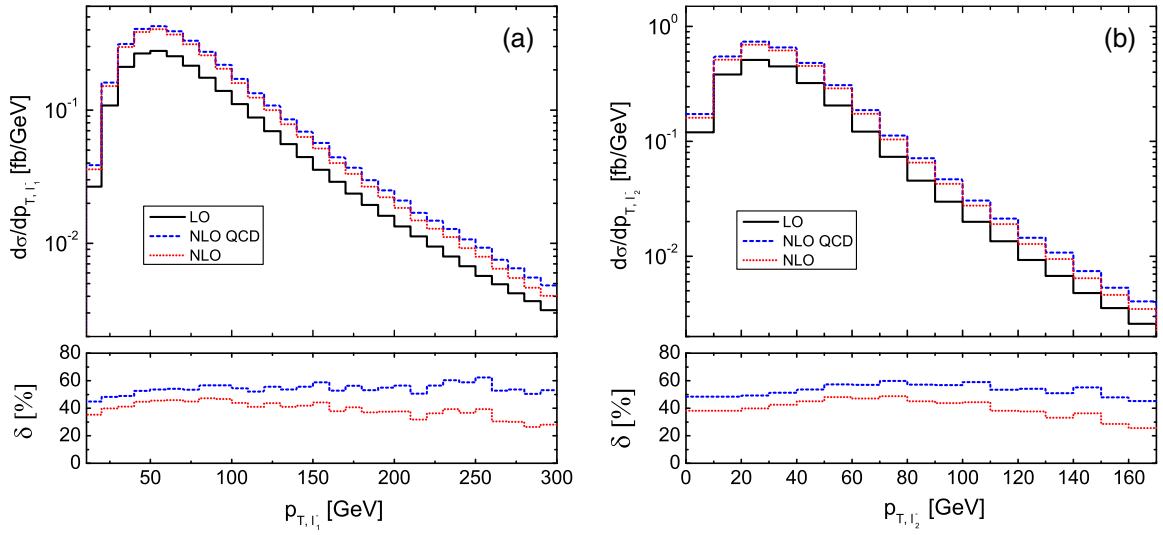

FIG. 8. The LO and NLO QCD and NLO QCD + EW corrected transverse momentum distributions of (a) leading and (b) second leptons for $pp \to ZZ + \text{jet} \to \ell^+\ell^-\ell'^+\ell'^- + \text{jet} + X$ at the 14 TeV LHC.

entangled in the Z-boson decays. In order to take into account the off-shell contribution and spin correlations from Z-boson leptonic decays, the MADSPIN method [30] implemented as a generic method in the MADGRAPH5 package framework is used to produce the decayed events. In practice, the data of final produced Z bosons with all needed information—such as the Born, virtual, and real emission contribution weights, external particle momenta, etc.—are recorded in standard format for the Les Houches Event Files [31] which can be automatically disposed by MADSPIN afterwards for the sequential Z-boson decays.

The MADSPIN method is an improved NWA based on the Frixione-Laenen-Motylinski-Webber (FLMW) [32] approach that performs well in preserving the spin correlation and finite-width effects. In the FLMW approach, the off-shell effect is recovered by smearing the mass of each resonance according to a Breit-Wigner distribution, and the spin correlation information is retained based on the acceptance-rejection method to generate the decay configurations. In determining whether a uniform decayed event is accepted or rejected in the NLO calculation, we should fix the maximum weight for kinematics X, $W_{\max}(X)$, which is a most important component in the FLMW procedure. In evaluating $W_{\max}(X)$ in MADSPIN, only the Born helicity amplitude is used approximately and the loop amplitude is ignored, while the hard emission amplitude is included. That means the spin correlation information is just retained in the tree-level accuracy. Some people have assessed the validity of the MADSPIN approach in some specific NLO QCD calculations, and found a good agreement with prediction by full NLO calculation. Therefore one makes a plausible assumption that "information from one-loop corrections in the production process are irrelevant as far as spin correlations are concerned" [30]. With regard to our work, we treat the final decayed events by adopting MADSPIN in the NLO EW calculation in the same way as in the NLO QCD calculation to preserve the spin correlation and finite-width effects as far as possible. Of course, a systematic study of the accuracy level in the EW NLO case needs further careful research.

In the interest of the effects from the spin correlation and finite width in Z-boson leptonic decays, we use two methods to generate tree-level decayed events and then give some LO distributions, and obtain the distributions presented in Figs. 6(a), 6(b), and 7 by adopting both methods for comparison, with the relative deviation shown in the lower panels defined as

$$\delta(x) = \left(\frac{d\sigma_{\text{MadSpin}}}{dx} - \frac{d\sigma_{\text{NWA}}}{dx}\right) \Big/ \frac{d\sigma_{\text{NWA}}}{dx}, \qquad (3.11)$$

where $x = p_{T,\ell_1^-}$, p_{T,ℓ_2^-} and $\phi_{\ell_1^-\ell_2^-}$. As shown in Fig. 6(a), the transverse momentum distribution of the leading lepton is enhanced by the spin correlation and finite-width effects when $p_{T,\ell_1^-} < 50$ GeV, while it is suppressed in the region of $p_{T,\ell_1^-} \in [50, 190]$ GeV, compared to the one obtained by using the naive NWA method. Correspondingly, the relative deviation can reach 6.21% at $p_{T,\ell_1^-} \sim 30$ GeV and −2.84% at $p_{T,\ell_1^-} \sim 90$ GeV in the plotted p_{T,ℓ_1^-} region. From Fig. 6(b) we see that the spin correlation and finite-width effects in the transverse momentum distribution of the second lepton are more apparent, and the relative deviation varies between 4.75% and −14.45% for p_{T,ℓ_2^-} in the range of $[0, 140]$ GeV. In analogy to the transverse momentum distributions of the final leptons, the distributions of the azimuthal-angle separation of the two negatively charged leptons depicted in Fig. 7 also demonstrate sizable spin correlation and finite width effects. The corresponding relative deviation varies from 2.17% to −2.36% in the

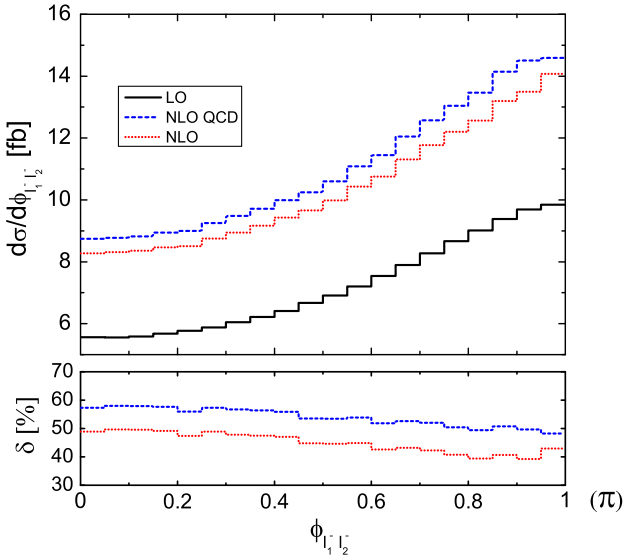

FIG. 9. The LO and NLO QCD and NLO QCD + EW corrected distributions of the azimuthal angle between the two negatively charged leptons for $pp \to ZZ + \text{jet} \to \ell^+\ell^-\ell'^+\ell'^- + \text{jet} + X$ at the 14 TeV LHC.

plotted $\phi_{\ell_1^-\ell_2^-}$ region. We can conclude from Figs. 6(a), 6(b), and 7 that the off-shell contribution and spin correlation from the Z-boson leptonic decays are non-negligible, and therefore should be considered in the NLO QCD + EW precision calculation.

In Figs. 8(a) and 8(b) we depict the LO and NLO QCD and NLO QCD + EW corrected transverse momentum distributions of the leading and second negatively charged leptons for $pp \to ZZ + \text{jet} \to \ell^+\ell^-\ell'^+\ell'^- + \text{jet} + X$ by adopting the MADSPIN method. The corresponding relative corrections are shown in the lower plots. We see from the figures that both the LO and NLO corrected p_{T,ℓ_1^-} distributions reach their maxima at $p_{T,\ell_1^-} \sim 60$ GeV, while the p_{T,ℓ_2^-} distributions peak at $p_{T,\ell_2^-} \sim 30$ GeV. The relative corrections for the transverse momentum distribution of ℓ_1^- exhibit similar behavior with ℓ_2^-. The relative QCD correction is fairly stable in the whole plotted p_T range. In contrast, the relative EW correction becomes significant in the high-p_T region, of about -16.3% at $p_{T,\ell_1^-} \sim 300$ GeV for the leading lepton and -14.1% at $p_{T,\ell_2^-} \sim 170$ GeV for the second lepton.

In Fig. 9 we present the LO and NLO QCD and NLO QCD + EW corrected distributions of the azimuthal angle between the two negatively charged leptons and the corresponding relative corrections for $pp \to ZZ + \text{jet} \to \ell^+\ell^-\ell'^+\ell'^- + \text{jet} + X$ by employing the MADSPIN method. From the figure we see clearly that the two negatively (as well as positively) charged leptons in the final state prefer to be back to back. The NLO QCD correction enhances the LO $\phi_{\ell_1^-\ell_2^-}$ distribution remarkably, and the relative QCD correction decreases from 57.3% to 48.2% with the increment of $\phi_{\ell_1^-\ell_2^-}$ from 0 to π. While the NLO EW correction suppresses the LO $\phi_{\ell_1^-\ell_2^-}$ distribution slightly, the relative EW correction is quite stable, varying in the range of $[-6.96\%, -5.24\%]$. Consequently, the full NLO relative correction varies from 49.7% to 39.3% in the plotted $\phi_{\ell_1^-\ell_2^-}$ region.

IV. SUMMARY

In this paper, we calculated the NLO QCD + NLO EW corrections to ZZ + jet production including subsequent Z-boson leptonic decays at the 14 TeV LHC. In dealing with the Z-boson leptonic decays, we employed the MADSPIN method to take into account the spin correlation and finite-width effects. Our numerical results show that the off-shell contribution and spin correlation from the Z-boson leptonic decays should be included in precision calculations. The NLO EW correction is relatively small compared to the NLO QCD correction, but it is non-negligible for precision theoretical predictions, particularly in high transverse momentum and invariant mass regions due to the Sudakov effect. Our analysis of the factorization/renormalization scale dependence of the integrated cross section affirms that the NLO QCD + EW correction can significantly reduce the scale uncertainty.

ACKNOWLEDGMENTS

This work was supported in part by the National Natural Science Foundation of China (Grant No. 11275190, No. 11375171, No. 11405173, No. 11535002, No. 11375008).

[1] J. Butterworth *et al.*, arXiv:1405.1067.
[2] G. Aad *et al.* (ATLAS Collaboration), J. High Energy Phys. 03 (2013) 128; Phys. Rev. Lett. **116**, 101801 (2016).
[3] S. Chatrchyan *et al.* (CMS Collaboration), J. High Energy Phys. 01 (2013) 063; Phys. Lett. B **721**, 190 (2013); V. Khachatryan *et al.* (CMS Collaboration), Phys. Lett. B **740**, 250 (2015).
[4] J. Ohnemus, Phys. Rev. D **50**, 1931 (1994); J. M. Campbell and R. K. Ellis, Phys. Rev. D **60**, 113006 (1999); L. J. Dixon, Z. Kunszt, and A. Signer, Phys. Rev. D **60**, 114037 (1999); F. Caola, K. Melnikov, R. Röntsch, and L. Tancredi, Phys. Rev. D **92**, 094028 (2015); arXiv:1605.04610.
[5] F. Cascioli, T. Gehrmann, M. Grazzini, S. Kallweit, P. Maierhöfer, A. von Manteuffel, S. Pozzorini, D. Rathlev,

L. Tancredi, and E. Weihs, Phys. Lett. B **735**, 311 (2014); M. Grazzini, S. Kallweit, and D. Rathlev, Phys. Lett. B **750**, 407 (2015).
[6] T. Matsuura and J. J. van der Bij, Z. Phys. C **51**, 259 (1991); C. Zecher, T. Matsuura, and J. J. van der Bij, Z. Phys. C **64**, 219 (1994); T. Binoth, N. Kauer, and P. Mertsch, arXiv: 0807.0024.
[7] A. Bierweiler, T. Kasprzik, and J. H. Kühn, J. High Energy Phys. 12 (2013) 071; J. Baglio, L. D. Ninh, and M. M. Weber, Phys. Rev. D **88**, 113005 (2013).
[8] S. Gieseke, T. Kasprzik, and J. H. Kühn, Eur. Phys. J. C **74**, 2988 (2014).
[9] B. Bedermann, A. Denner, S. Dittmaier, L. Hofer, and B. Jager, Phys. Rev. Lett. **116**, 161803 (2016).
[10] T. Binoth, T. Gleisberg, S. Karg, N. Kauer, and G. Sanguinetti, Phys. Lett. B **683**, 154 (2010).
[11] T. Hahn, Comput. Phys. Commun. **140**, 418 (2001).
[12] T. Hahn and M. Perez-Victoria, Comput. Phys. Commun. **118**, 153 (1999).
[13] G. J. van Oldenborgh, Comput. Phys. Commun. **66**, 1 (1991).
[14] J. Alwall, R. Frederix, S. Frixione, V. Hirschi, F. Maltoni, O. Mattelaer, H.-S. Shao, T. Stelzer, P. Torrielli, and M. Zaro, J. High Energy Phys. 07 (2014) 079.
[15] A. Denner, Fortschr. Phys. **41**, 307 (1993).
[16] A. Sirlin, Phys. Rev. D **22**, 971 (1980).
[17] A. Denner and S. Dittmaier, Nucl. Phys. **B658**, 175 (2003).
[18] G. Passarino and M. Veltman, Nucl. Phys. **B160**, 151 (1979).
[19] D. T. Nhung, L. D. Ninh, and M. M. Weber, J. High Energy Phys. 12 (2013) 096.
[20] J.-J. Su, W.-G. Ma, R.-Y. Zhang, S.-M. Wang, and L. Guo, Phys. Rev. D **78**, 016007 (2008).
[21] K.-P. O. Diener, S. Dittmaier, and W. Hollik, Phys. Rev. D **72**, 093002 (2005).
[22] B. W. Harris and J. F. Owens, Phys. Rev. D **65**, 094032 (2002).
[23] A. Denner, S. Dittmaier, T. Kasprzik, and A. Muck, J. High Energy Phys. 08 (2009) 075; 06 (2011) 069; A. Denner, S. Dittmaier, T. Gehrmann, and C. Kurz, Nucl. Phys. **B836**, 37 (2010).
[24] E. W. N. Glover and A. G. Morgan, Z. Phys. C **62**, 311 (1994).
[25] D. Buskulic *et al.* (ALEPH Collaboration), Z. Phys. C **69**, 365 (1995).
[26] K. A. Olive *et al.* (Particle Data Group), Chin. Phys. C **38**, 090001 (2014).
[27] R. D. Ball, V. Bertone, S. Carrazza, L. Del Debbio, S. Forte, A. Guffanti, N. P. Hartland, and J. Rojo (NNPDF Collaboration), Nucl. Phys. **B877**, 290 (2013).
[28] A. Denner, S. Dittmaier, M. Hecht, and C. Pasold, J. High Energy Phys. 04 (2015) 018.
[29] A. Denner and S. Pozzorini, Eur. Phys. J. C **18**, 461 (2001); **21**, 63 (2001).
[30] P. Artoisenet, R. Frederix, O. Mattelaer, and R. Rietkerk, J. High Energy Phys. 03 (2013) 015.
[31] E. Boos *et al.*, arXiv:hep-ph/0109068; J. Alwall *et al.*, Comput. Phys. Commun. **176**, 300 (2007).
[32] S. Frixione, E. Laenen, P. Motylinski, and B. R. Webber, J. High Energy Phys. 04 (2007) 081.